Role of H 3 + ions in deposition of silicon thin films from SiH 4 /H 2 discharges: modeling and experiments

Tinghui Zhang, Jean-Maxime Orlac'h, Monalisa Ghosh, Vincent Giovangigli, Pere Roca I Cabarrocas, Tatiana Novikova

Role of H$_3^+$ ions in the deposition of silicon thin films from SiH$_4$/H$_2$ discharge: modeling and experiments

Tinghui Zhang[1], Jean-Maxime Orlac'h[2], Monalisa Ghosh[1], Vincent Giovangigli[3], Pere Roca i Cabarrocas[1] ,Tatiana Novikova[1]

[1]Laboratoire de Physique des Interfaces et des Couches Minces, Ecole Polytechnique, IP Paris 91120, Palaiseau, France
[2]ONERA, DAAA-CLEF, 92320, Châtillon, France
[3]Centre de Mathématiques Appliquées, Ecole Polytechnique, IP Paris 91120, Palaiseau, France

E-mail: tatiana.novikova@polytechnique.edu

Abstract

A 1D fluid model of silane-hydrogen discharges that includes a detailed chemistry of gas phase and surface reactions to account for deposition and etching processes has been implemented to study the effects of gas pressures (1 to 3.5 Torr) and silane concentration (2 to 10%) on the deposition rate of silicon thin films in a standard RF-PECVD reactor. The thickness of the films and their deposition rate as functions of the process conditions were determined from the spectroscopic ellipsometry measurements in UV-visible wavelength range. The experimental values of the deposition rate were compared with the results obtained from the 1D fluid model. SiH$_3$ radicals are found to be the main contributors to the computed deposition rates, while H$_3^+$ ions play the main role in the etching process. The study reveals that etching by hydrogen ions must be taken into account to reproduce correctly the experimental deposition rate. In particular etching by H$_3^+$ ions must be taken into account to achieve a good agreement between the experimental and modelled values of the deposition rate as a function of the total gas pressure and the silane fraction in the gas phase.

1. Introduction

Plasma-enhanced chemical vapor deposition (PECVD) [1-3] has been studied for over 40 years as it is widely used for growing a variety of silicon thin films, ranging from hydrogenated amorphous silicon (a-Si:H) to microcrystalline (μc-Si:H) and even crystalline silicon (c-Si) epitaxial films for various applications in large-area electronics, optoelectronics, and photovoltaics. For silicon thin film deposition in capacitively coupled radio frequency (RF) discharges, the growth rate and film properties are strongly affected by the plasma process parameters, e.g., silane concentration, gas pressure, RF power, excitation frequency, and inter-electrode distance. Though there is a general consensus on SiH$_3$ radicals being the main film precursors under standard PECVD conditions, i.e. low pressure (< 100 mTorr) and low RF power (~10 mW/cm^2) [4], other precursors such as silicon clusters (Si$_n$H$_m$) may also play a role as well as etching by atomic hydrogen, H$_2^+$ and H$_3^+$ ions [5]. However, the processes taking place in silane/hydrogen discharges, including plasma chemistry and plasma-surface interactions, are complex and still not fully understood. In particular, the fine details of the growth mechanism remain unclear.

Modeling of silane-based plasmas has been widely applied to understand the plasma dynamics and chemistry and to determine the contribution of different species to the growth [6-10]. However, most of these studies are related to the low-pressure conditions and are not representative of the high pressure regime in which we are interested in for the deposition of polymorphous silicon thin films on glass substrates and Si epitaxial growth on c-Si [11,12].

Nevertheless, a few groups have studied such high pressure conditions. The group of D. Mataras developed an experiment-based chemical kinetic-mass transfer model and used it to simulate the deposition of μc–Si:H in highly diluted SiH_4 in H_2 discharge [13]. Besides the 38 gas phase reactions considered, their model also considers a set of surface chemical reactions based on three types of surface sites: dangling bond sites, H covered sites and SiH_3 physisorbed sites. For each radical the reaction probabilities with different surface sites are taken into account, for example, the reaction probability of both SiH_3 and Si_2H_5 radicals with the dangling bond sites set to be equal to 1 whereas with H covered sites it is set to be equal to 0.5. The values of sticking coefficients σ of both SiH_3 and Si_2H_5 radicals are consistent with those cited by J. Perrin [14-16]. Under the high pressure of 1 Torr and 6 % SiH_4 of silane concentration in H_2 the simulated deposition rate of μc–Si:H film increases from 1 Å/s to 7 Å/s with the increase of power density (10-70 mW/cm^2). They also reported Si_2H_4, SiH_3 and SiH_2 radicals to be the main precursors for the film depostion, while the etching rate by H atoms was found to be negligible. Later a hybrid kinetic Monte Carlo method [17] was presented to simulate the impact of the variation of silane fraction from 1% to 6% on the growth of nanocrystalline silicon in silane/hydrogen discharge at 3 Torr and 310 mW/cm^2 RF power. In [17] five species (H, SiH_3, SiH_2, SiH and Si_2H_5), that contribute to 29 surface reactions with different surface sites, are taken into account to model the surface chemistry. The computed deposition rate increases with silane fraction that reproduces the experimental trend, but there is a discrepancy of about 2 Å/s in deposition rate values between the simulations and experiments.

The main contribution to silicon thin film deposition comes from the radicals in numerical studies. However, few researchers have considered the significance of ion species in the competing deposition and etching processes in silane/hydrogen discharges. L.L. Alves [18] studied the contribution of radicals and ions to the deposition of a-Si:H films using a fluid model of RF discharge under conditions of very high silane concentration and low gas pressure (83% SiH_4, 68 mTorr and 60% SiH_4, 68 mTorr). The loss probabilities l and sticking coefficient σ of SiH_3 and Si_2H_5 radicals were taken from [14-16], while $l = \sigma = 0.6$ was assumed for SiH_2 and Si_2H_4 radicals. The ion loss

possibilities were taken equal to unity. They found that thin film deposition is controlled by the fluxes of SiH_3 and SiH_2 radicals, while the contribution of ions (mainly SiH_3^+ and SiH_2^+) to deposition is about 9%. In addition, the simulated deposition rates show a good agreement with the experiments. O. Leroy [7] also studied the role of ions in deposition and etching of a-Si:H films by using a 2D fluid model under low-pressure conditions (9 Pa and 40 Pa). For the surface processes, the loss probability l and sticking coefficient σ of radicals were taken from [14-16]. The SiH_m^+ and H_2^+ ions are considered in surface chemistry processes with a loss probability $l = 1$, whereas H^+ and H_3^+ ions are excluded. According to their results the main film precursors are SiH_3 and SiH_2 radicals, while SiH_m^+ ions account for less than 10% of deposition rate. The H_2^+ ions related etching rate is found negligible under these conditions. However, these studies on ions contribution to the silicon thin film deposition rate are not performed in a high-pressure regime which we are interested in.

This work is focused on the comparison between the experimental and simulated deposition rates in a SiH_4/H_2 plasma discharge within relatively high pressure range (1.0 - 3.5 Torr) and at low silane concentration (2 – 10% silane in hydrogen). These conditions lead to the growth of polymorphous silicon on glass substrate and epitaxial growth on (100) oriented crystalline silicon substrate [1]. The 1D fluid model includes Poisson's equation, the transport and drift-diffusion equations with the appropriate boundary conditions for the ions, radicals, molecules and electrons, the corresponding transport parameters, the reaction rates, the equation for electron energy as well as the gas-phase and surface chemistry. In particular, the surface chemistry (including the recombination, etching, and deposition reactions) is coupled to the fluid model via a set of reaction probabilities. The net deposition rate from the model is compared to that obtained experimentally and the main species contributing to deposition and etching are identified.

In the section 2, the experimental setup and process parameters are presented. The 1D fluid model is presented in details in the section 3, before moving to the comparison and discussion on simulated and experimental deposition rates for the two series of experiments in the section 4.

2. Experimental setup and parameters

A capacitively coupled parallel plate reactor, having a base vacuum of 10^{-7} mbar, was used for silicon thin film deposition [19]. Fig.1 shows a schematic representation of the axisymmetric reactor. The silane-hydrogen gas mixture is injected through the showerhead of the RF electrode with a diameter of 15 cm as shown in the Fig.1. The upper electrode carrying the substrates is grounded and the gases are pumped via a slit between the substrate holder and a plasma box that confines the discharge between the two electrodes.

In this work the (100) c-Si wafers and Corning glass were used as the substrates for the silicon thin film deposition. For the series of experiments with varying silane concentration, the hydrogen flow rate was fixed at 500 sccm and the silane flow rate was varied whereas the total pressure was kept constant at 2 Torr. For the pressure series experiments the gas flow rate of silane and hydrogen was kept constant at 7 sccm and 500 sccm, respectively, whereas the total pressure was varied by changing the pumping rate of the gases using butterfly valve. From the *ex situ* spectroscopic ellipsometry measurements it has been evidenced that polymorphous silicon films [20] are deposited on the glass substrates while on c-Si substrates the deposited films are microcrystalline. The thickness of silicon thin films was determined from the fit of spectroscopic ellipsometry measurements using Tauc-Lorentz model for the polymorphous silicon films deposited on glass substrates [20] and Bruggeman effective medium approximation model for the microcrystalline and epitaxial films deposited on c-Si substrates [21]. The corresponding deposition rates are calculated by dividing the measured thickness by the deposition time.
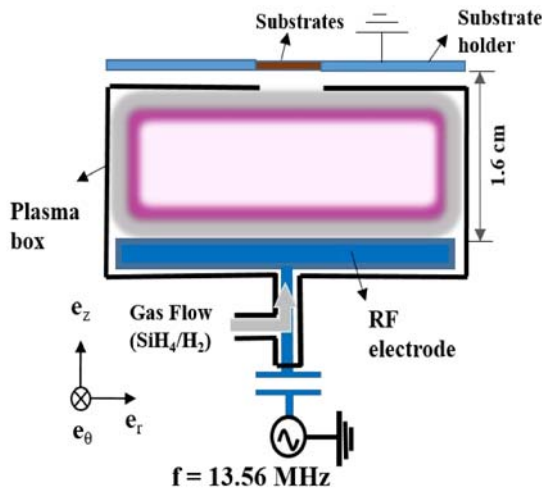

Figure 1. Schematic representation of the cross-section of axisymmetric RF plasma reactor.

3. Description of the model

A 1D fluid model is employed to describe silane/hydrogen RF plasma discharges. This model consists of the Poisson's equation for the electric potential coupled with a set of drift-diffusion and transport equations for charged and neutral species, respectively. The electron temperature is calculated self-consistently by solving an electron energy equation. The model has been previously validated for H_2 plasma discharges [22]. Since then it has been enriched with the silane/hydrogen gas-phase chemistry and surface chemistry to compute the deposition, recombination and etching rates. The coupling of the deposition and etching processes with plasma dynamics and its impact on the net deposition rate is studied through numerical simulations. The results of modeling are compared with the experimental data.

3.1 Conservation equations

Fluid models have been frequently used for the simulations of low-temperature RF plasma discharges with a low degree of ionization ($10^{-4} – 10^{-6}$) in gas mixtures such as H_2 with SiH_4, in a pressure range from few tens of mTorr to few Torr [23-25]. The equations describing spatio-temporal evolution of the species mass fractions and electron temperature are as follows:

$$\partial_t(\rho Y_k) + \partial_z(\rho Y_k v + \rho Y_k V_k) = W_k \dot{\omega}_k, k \in \mathsf{C}, \tag{1}$$

$$\partial_t \rho + 2\rho\alpha\tilde{u} + \partial_z \tilde{v} = 0 \tag{2}$$

$$\rho\, \partial_t \tilde{u} + \tilde{v}\, \partial_z \tilde{u} = \alpha(\rho^{in} - \rho\tilde{u}^2) + \partial_z(\eta\partial_z\tilde{u}) \tag{3}$$

$$\partial_t \left(\frac{3}{2}n_e k_B T_e\right) + \partial_z Q_e = n_e q_e V_e E + \dot{E}_{eh}. \tag{4}$$

Eq. 1 represents the continuity equations for each species. Here, ρ represents the mass density of the fluid mixture, $v = \rho\tilde{v}$ is the normal component of the macroscopic fluid velocity, $u = r\alpha\tilde{u}$ is the tangential velocity, α is the strain rate, C is the set of chemical species considered (electrons, ions, radicals, and molecules), Y_k denotes the mass fraction of the kth species, V_k denotes the diffusion velocity of the kth species. W_k is its molar mass, and $\dot{\omega}_k$ is its molar production rate. Eq.2 is the conservation equation for the fluid density, which determines the normal velocity v. Here, α is the strain rate, which is defined as $\alpha = \sqrt{\frac{J}{\rho^{in}}}$. J is the pressure curvature - a natural parameter of a laminar flow process that is generally independent of time. Eq.3 is the conservation equation for the tangential velocity. ρ^{in} is the mass density of injected mixture. η is the shear viscosity. Eq.2 and Eq.3 are taken from [26,27]. Eq.4 is the second moment of the Boltzmann equation for the electron probability density function, which describes the energy balance for electrons. Here, T_e is the electron temperature, Q_e denotes the electron heat flux, $n_e q_e V_e$ is the electron conduction current density, and $\dot{E}_{eh}$ is the energy exchange rate between the electrons and heavy species due to the inelastic collisions. Since the temperature of heavy species is assumed to be constant in the discharge, the corresponding equation for their energy balance is not resolved.

The electric potential φ is obtained by solving the Poisson's equation

$$\partial_z^2 \varphi = -\frac{nq}{\varepsilon_0} \tag{5}$$

where $n = \sum_{k \in \mathsf{C}} n_k$ is the mixture number density, $q = \sum_{k \in \mathsf{C}} \frac{q_k n_k}{n}$ is an average charge of the mixture, and $E = -\partial_z\varphi$ is the electric field. The magnetic field can be neglected because the discharge dimensions are too small compared to

the wavelength of the excitation RF signal with the frequency of 13.56 MHz. These fluid plasma equations are solved in a one-dimensional approximation to obtain the plasma macroscopic properties along the reactor axis. The thermodynamic properties of the neutral species are taken from [28].

3.2 Transport fluxes

The species diffusion velocities in Eq.1 can be written as:

$$V_k = -D_k \frac{\partial_z Y_k}{Y_k} + \mu_k \vec{E}, k \in \mathsf{C}, \tag{6}$$

where D_k is the diffusion coefficient and μ_k is the mobility coefficient of the kth species. Eq.6 is a simplified version of the classical Hirschfelder-Curtiss approximation [26,27] in a neutral gas mixture. For each species, the first term in Eq.6 represents diffusion velocity, and the second term is for drift velocity. For simplicity, we use the expression $\partial_z Y_k/Y_k$ instead of $\partial_z X_k/X_k$, where $X_k = Y_k \overline{m}/m_k$ is the mole fraction of the kth species.

The electron heat flux reads

$$Q_e = \frac{5}{2} n_e k_B T_e V_e - \lambda_e \partial_z T_e, \tag{7}$$

where λ_e is the electron thermal conductivity. The first term represents the transport of electron energy through diffusion, the second term describes the electron heat conduction. The Dufour and Soret effects [29] are negligible in our conditions.

3.3 Transport coefficients

The diffusion coefficients $D_k, k \in C$, are computed as in [27,28]:

$$D_k = \frac{p(1-Y_k)}{\sum_{l \in N, l \neq k} p_l / D_{k,l}^{bin}}, k \in C, \tag{8}$$

where p is the pressure of gas mixture, p_l is the partial pressure of lth species, $D_{k,l}^{bin}$ is the binary diffusion coefficient for the species pair (k, l), and $N \subset C$ denotes the set of neutral species. For neutral species we use Lennard-Jones potential to calculate $D_{k,l}^{bin}$. EGLIB software [30] is employed to calculate the transport coefficients. Collision integrals are computed using the 'TRANFT' fitting program [31].

Since the densities of both charged species and radicals are much smaller than the densities of H_2 and SiH_4 ($Y_k \ll 1$, low degree of ionization and dissosiation) that are the main species, we consider the diffusion of the charged species against H_2 and SiH_4 only. For the electron collisions we use BOLSIG+ software [32] to obtain the electron diffusion coefficient D_e and electron mobility coefficient μ_e, using the input cross-sections data of electron-collision reactions listed in [33-44] and our process conditions (gas temperature, gas composition, *etc*). As the composition of gas mixture (% SiH_4, % H_2) does not change significantly in the

discharge, we run BOLSIG+ offline for a given silane mole fraction, and tabulate the values of electrons transport coefficients as a function of electron temperature only.

The binary diffusion coefficients of ions against the neutral molecules are computed according to Langevin theory [14]:

$$D_{ij}^{bin} p = 5.2 \times 10^{-3} \frac{k_B T_h}{|q_i|} \frac{T}{\sqrt{\delta_j m_{ij}}} \, cm^2 s^{-1} torr \tag{9}$$

where p is the pressure, k_B is the Boltzmann constant, T is the gas temperature, q_i is the charge of ith species, m_{ij} is the reduced mass (atomic mass units) $m_{ij} = m_i m_j/(m_i + m_j)$, and δ_j is the polarizability of gas molecule [14]:

$$\delta_{H_2} = 0.805 \text{Å}^3, \ \delta_{SiH_4} = 4.62 \text{Å}^3 \tag{10}$$

For the binary mobility coefficients of ions, we use Einstein relation:

$$\mu_{ij} = \frac{q \, D_{ij}}{k_B T} \tag{11}$$

The ion mobility of species i is calculated from the mobility μ_{ij} in each gas species j through the expression:

$$\frac{1}{\mu_i} = \sum_j \frac{P_j/P}{\mu_{ij}} \tag{12}$$

3.4 SiH₄-H₂ plasma chemistry

Our plasma chemistry model takes into account 19 species listed in Table 1, including the species with Si that contain up to 2 silicon atoms. The model calculates each species' density and flux along the reactor axis towards the electrodes.

The gas phase chemistry model includes two types of reactions: the electron collision reactions and the heavy species reactions. We consider 24 electron collision reactions and 19 heavy species reactions. The full list of reactions is provided in the Annex I and Annex II

Table 1. Species included in the fluid model

Neutral species	H_2, SiH_4, H, SiH_3, SiH_2, H_3SiSiH, Si_2H_5, Si_2H_6
Charged species	SiH_3^+, SiH_2^+, $Si_2H_4^+$, H_3^+, H_2^+, H^+, e, SiH_2^-, SiH_3^-, $Si_2H_5^-$, H_3SiSiH^-

The reaction rates are calculated using a generalized Arrhenius form:

$$K_r^f(T_r) = A_r T_r^{\beta_r} exp\left(-\frac{\mathfrak{E}_r}{RT_r}\right) \tag{13}$$

where T_r is the temperature of the rth reaction, namely $T_r = T$ for heavy species reactions and $T_r = T_e$ for electron collision reactions, A_r is the pre-exponential factor, β_r is the exponent of temperature and $\mathfrak{E}_r > 0$ is the activation energy of the rth reaction.

The calculations of the deposition and etching rate are based on the evaluation of each species' contribution. The net deposition rate is determined from the difference between the computed deposition and etching rates and is compared with experimental data.

3.5 Boundary conditions

The secondary electron emission induced by the bombardment of electrodes by the flux of positive ions under PECVD conditions in silane/hydrogen discharge is considered. The coefficient of secondary electron emission is taken as $\gamma_e = 0.1$ [45]. The electric potential is set to zero at the grounded electrode, whereas a sine excitation voltage waveform is applied at the powered electrode. It has been checked that, for the process conditions studied in this work, the experimentally measured values of the DC self-bias at the powered electrode have negligible effect on the deposition rate in our numerical simulations. Therefore, there was no DC self-bias taken into account in our model. The boundary conditions for electron density, electron temperature and electron energy flux are taken from [22].

For all non-negative species, the boundary conditions at both electrodes are written as:

$$\left(\rho Y_k \vec{V}_k \cdot \vec{n}\right)\big|_{t,0} = W_k \dot{\omega}_k, k \in N \cup P, \quad (14)$$

where P represents the set of positive ions, N represents the set of neutral species, $\vec{n}$ is the unit vector normal to the electrode's surface pointing outwards from the reactor, $\dot{\omega}_k$ is the net molar surface loss rate of the kth species that is calculated from the surface reaction rates $\dot{\tau}_r$, $r \in \hat{R}$, as:

$$\dot{\omega}_k = \sum_{r \in \hat{R}} \left(v_k^{rf} - v_k^{rb}\right) \dot{\tau}_r, \ k \in N \cup P. \quad (15)$$

where $\hat{R}$ denotes the set of surface species reactions, and v_k^{rf} and v_k^{rb} denote the forward and backward stoichiometric coefficients for the kth species in the rth surface reaction, respectively.

Since the negative ions are trapped in the plasma, their densities are set as zero at both boundaries. On the contrary, the positive ions are accelerated through the plasma sheaths, eventually contributing to the surface processes. Neutral species also contribute to the surface chemistry. Finally, the boundary conditions for the electrons take into account the secondary emission process, and will be detailed below.

Each surface reaction $r \in \hat{R}$ is associated with a unique gas-phase heavy species reactant, namely, an ion or a neutral species. The net molar surface loss rate of the kth species impinging on the surface is computed from the outward mass flux $F_k|_{\text{out}}$ of species k as follows:

$$\dot{\omega}_k = \frac{l_k F_k|_{\text{out}}}{W_k} \quad (16)$$

where l_k is the loss probability of the kth impinging species: in particular $l_k = 0$ if the species is specularly reflected at the surface, and $l_k = 1$ if the species is completely lost due to either sticking, recombination or etching reaction.

The outward mass flux for each species (electron, neutral, or positive ion) is computed as:

$$F_k|_{\text{out}} = \rho Y_k \max\left[\vec{V}_k^{drift} \cdot \vec{n}, \ V_{k+}\right], \ k \in P \cup N \cup \{e\}, \quad (17)$$

where $\vec{V}_k^{drift}$ is the drift velocity of the kth species that reads:

$$\vec{V}_k^{drift} = \mu_k \vec{E}, \quad k \in C, \quad (18)$$

where V_{k+} is the average velocity of kth species towards electrodes computed as that of a Maxwellian distribution function, that is [46]

$$V_{k+} = \frac{1}{2} v_k^{th} = \left(\frac{8 R T_k}{\pi W_k}\right)^{\frac{1}{2}}, k \in C \quad (19)$$

We assume that the mobilities of neutral species are equal to zero. It follows from Eq.17 that if the outwards drift velocity $\vec{V}_k^{drift}$ is larger than the thermal velocity v_k^{th}, the outward flux at the boundary is equal to the drift velocity, however, when the drift velocity is smaller or oriented inwards the discharge, the diffusion velocity at the electrode is equal to the thermal velocity. It guarantees that the flux of positive ions is always pointing outwards the reactor. Note that for neutral species the outward flux is simply the thermal flux.

3.6 Surface processes

For silane/hydrogen plasma discharges, the surface processes for species reaching the reactor walls consist of reflection, recombination, sticking and etching reactions, as shown in Fig.2. When a species reaches the substrate, there is a certain probability for each type of surface reaction.
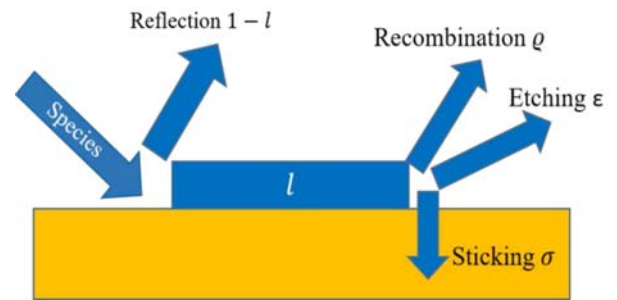

Figure 2. Schematic representation of the surface processes in silane/hydrogen plasma.

For each species $k \in N \cup P$ impinging (and reacting) on the surface, three kinds of reactions may occur, namely sticking, recombination or etching. When the gas species $SiH_x(g)$ stick to the surface we consider that they contribute to film growth. The etching reactions take Si atoms away from surface, resulting in the formation of the volatile species $SiH_x(g)$, while the surface recombination of gas

Tinghui Zhang *et al*

phase species contributes neither to deposition nor to etching processes (e.g. H(g) + wall = 0.5H$_2$(g)).

One should note that it is possible – though it does not happen in our case – that several reactions of the same type occur, e.g. SiH$_3$ could be involved in two types of recombination reaction (SiH$_3$(g) + SiH$_3$-wall = Si$_2$H$_6$(g) and SiH$_3$(g)+H-wall=SiH$_4$(g)). Still, for a given impinging species k, the sum of the probabilities of all reactions is always equal to the loss probability l_k, the remainder of the molecules being specularly reflected with a probability $1 - l_k$. In other words:

$$0 \leq l_k = \sigma_k + \varrho_k + \varepsilon_k \leq 1 \qquad (20)$$

where l_k is the loss probability, and where σ_k, ϱ_k and ε_k are the the sticking, recombination and etching probabilities, respectively. The rate of progress of reaction $r \in \hat{R}$ (which is either a sticking, a recombination or an etching reaction) is then calculated as:

$$\dot{\tau}_r = \frac{p_r}{(1 - \frac{l_k}{2})} \frac{\dot{\omega}_k}{v_k^{rf}}, \quad r \in \hat{R} \qquad (21)$$

where p_r is the probability of reaction r, that is $p_r = \sigma_k$ if r is a sticking reaction, $p_r = \varrho_k$ if r is a recombination reaction, and $p_r = \varepsilon_k$ if r is an etching reaction. The denominator $1 - \frac{l_k}{2}$ ensures the validity of Eq.21 in the limit $l_k \to 1$, where nearly all the molecules of species k are lost at the wall and no molecules are specularly reflected, in which case the distribution function of the kth species close to the wall is strongly anisotropic [47-49]. Note that for positive ions the loss probability is always 1.0 in our model.

The deposition rate of silicon thin film associated with each surface reaction r then follows

$$v_{\text{Si(s)}}^r = V_m^{\text{Si}} v_{\text{Si(s)}}^{rb} \dot{\tau}_r > 0, \qquad (22)$$

where $v_{\text{Si(s)}}^{rb}$ is the backward stoichiometric coefficient of Si(s) in the rth surface reaction, and V_m^{Si} is the molar volume of crystalline silicon $V_m^{\text{Si}} \cong 12.06 \text{ cm}^3 \cdot \text{mol}^{-1}$. The etching rate of silicon thin film associated with each surface reaction r reads similarly

$$v_{\text{Si(s)}}^r = -V_m^{\text{Si}} v_{\text{Si(s)}}^{rf} \dot{\tau}_r < 0,$$

and, consequently, the net deposition rate of silicon thin film reads

$$v_{\text{Si(s)}} = \sum_{r \in \hat{R}} v_{\text{Si(s)}}^r. \qquad (23)$$

The total deposition rate considers the sticking reactions only. The list of the surface reactions and the corresponding probabilities are given in the Annex III.

Finally, the boundary conditions for electrons read:

$$\left(\rho Y_e \vec{V}_e \cdot \vec{n} \right)|_{t,0} = F_e|_{\text{out}} - W_e \sum_{k \in P} \gamma_e \frac{F_k|_{\text{out}}}{W_k} \qquad (24)$$

where γ_e is the secondary electron emission coefficient.

3.7 Numerical implementation

The spatial discretization of the Equations (1)-(5) is obtained by applying a three-point finite difference scheme. The drift-diffusion equations for species mass fractions and electron temperature are dealt with using the Scharfetter-Gummel discretization scheme [50-51]. The time derivatives of Equations (1) and (4) are discretized in a fully implicit manner and solved by Newton method by using Euler predictor [52].

In our simulations, the RF frequency of the excitation signal is equal to 13.56 MHz. Reaching the steady-state for silane/hydrogen plasmas requires the simulation of about 40000 RF cycles, and each RF cycle is resolved with a time step of 2.5×10^{-10} s. Typical calculation time for 40000 RF is about two weeks on our PC (Intel(R) Xeon(R) Silver 4214 CPU @ 2.2GHz, 48 cores, RAM: 64GB). The criterion of convergence for the deposition rate in the model is given by

$$\left| \frac{v_{\text{Si(s)}}^{ncyc+100} - v_{\text{Si(s)}}^{ncyc}}{100} \right| \ll 1 \times 10^{-5} \qquad (25)$$

where *ncyc* is the number of RF cycles.

4. Results and Discussion

4.1 Impact of silane concentration on deposition rate

In the following, we address the effect of silane concentration on the deposition rate. The reactor geometry and process conditions are defined as follows: the gas temperature is fixed at 448K, the pressure is equal to 2 Torr, the dissipated RF power is fixed at 30 W, the inter-electrode distance is equal to 1.6 cm, and the silane mass concentration (SiH$_4$/(SiH$_4$+H$_2$)) is varied from 2% to 10%. Increasing silane concentration is obtained by increasing the silane flow rate while keeping the H$_2$ flow rate fixed at 500 sccm (see [53]).

Fig.3(a) shows the computed deposition rate (black triangles) compared with the corresponding experimental values (red circles) taken from [53] as a function of silane concentration. As we can see, the model reproduces the trend in deposition rate, but there is a discrepancy in the absolute values, in particular, in the low silane concentration range. The contribution of species such as SiH$_3$, SiH$_2$, Si$_2$H$_5$, and H$_3$SiSiH to the total deposition rate is also shown in this figure. The SiH$_3$ radicals are found to be the main precursor for the film growth and their contribution increases with the silane concentration in a gas mixture. For the given process conditions, other reactive species considered in the model (see Table I) have a negligible contribution to the deposition rate. Note that the contribution of Si$_2$H$_5$ and H$_3$SiSiH radicals also increases with silane concentration, whereas the contribution of SiH$_2$ radicals to the deposition rate decreases. Such behavior is the result of the secondary reactions (R4, R7, R11 and R12 in the annex II) that become important at
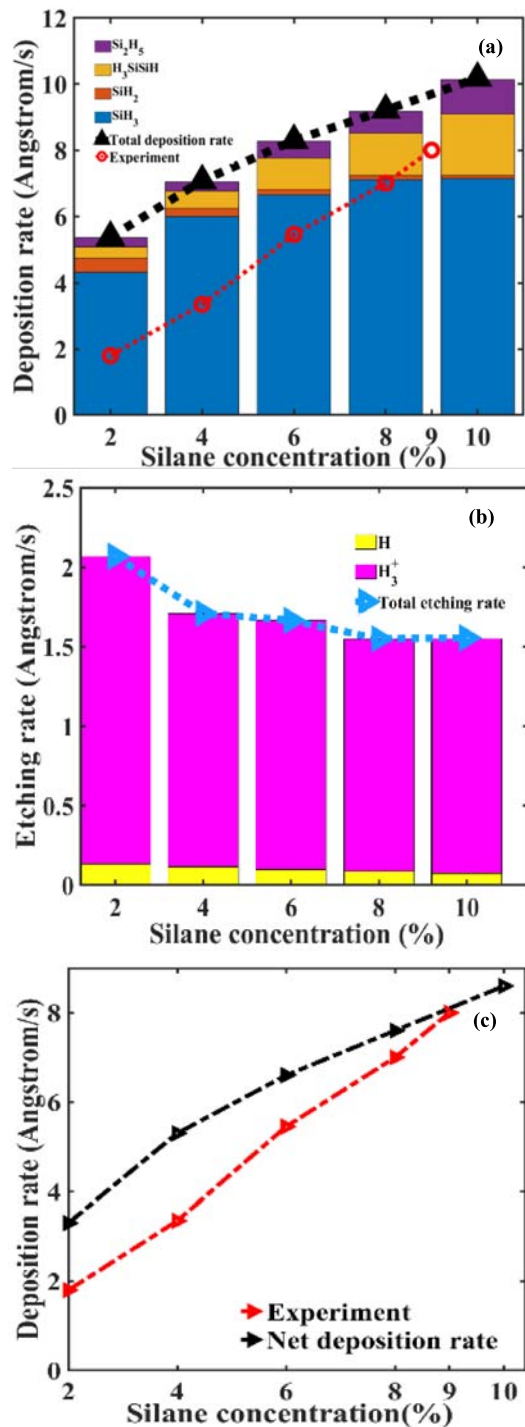
Figure 3. Deposition and etching rates versus silane concentration: (a) simulated deposition rate (black triangles) and experimental data (red circles), the histogram shows the contribution of main species to the deposition rate; (b) simulated etching rate, the histogram shows the contribution of H and H_3^+ to the etching rate; (c) simulated net deposition rate (black triangles), experimental values (red triangles).

pressure 2 Torr. The contribution of ions to the deposition is negligible compared to radicals; for example, SiH_3^+ ions

cover the range from 0.022 Å/s at 2% silane concentration to 0.038 Å/s at 10% silane concentration that is less than 1% of the computed total deposition rate

Note that the difference in deposition rate between the model and experiments becomes smaller as silane concentration increases. To explain this difference, we consider the etching by hydrogen species that will reduce the computed net deposition rate. Previous numerical studies have shown that etching by both atomic hydrogen and hydrogen ions has a negligible effect [7,13], while experimental studies have shown that etching does take place in RF hydrogen plasmas [5,54,55]. Fig.3(b) presents the total etching rate as a function of silane concentration. The increase of silane concentration results in a decrease in the total etching rate from 2.07 Å/s at 2% silane to 1.55 Å/s at 10% silane. O. Leroy [7] suggested that the main precursor of etching is H_2^+, however, as can be seen in Fig.3 (b), H_3^+ ions make over 90% of the etching rate that shows a decreasing trend as silane concentration increases. For atomic hydrogen, the etching rate is much smaller compared to the H_3^+ etching rate that varies from 0.07 Å/s to 0.14 Å/s in the studied silane concentration range. The net deposition rate is determined as the difference between the computed deposition and etching rates. The comparison between the calculated net deposition rate and the corresponding experimental values is presented in Fig.3(c). We can see that the net deposition rate comes closer to the experimental values.

The dominant contribution of the SiH_3 radicals and H_3^+ ions to the computed deposition and etching rates, respectively, can be traced back to the fluxes of the species towards the substrate Fig.4(a) shows the fluxes of various species towards the substrate as a function of silane concentration. It is clearly seen that the flux of SiH_3 radicals is much larger compared to the fluxes of other radicals and ions. It indicates that SiH_3 radicals are the main precursors of silicon thin film deposition, even if its sticking coefficient (0.1) is lower than that of SiH_2 (0.8) and H_3SiSiH (0.8). As we can see, the increase in silane concentration is followed by an increase in SiH_3 fluxes, from 5.5×10^{15} cm^{-2}·s^{-1} at 2% of silane to 8.8×10^{15} cm^{-2}·s^{-1} at 8% of silane, and then by a slight decrease to 8.5×10^{15} cm^{-2}·s^{-1} at 10% silane. The trend in SiH_3 radical flux with silane concentration in Fig.4(a) reflects the trend of SiH_3 deposition rate with silane concentration in Fig.3(a). Fig.4(b) shows the fluxes of SiH_2 and higher silane species (Si_2H_5 and H_3SiSiH) versus silane concentration. The decrease of SiH_2 flux and the increase of both Si_2H_5 and H_3SiSiH fluxes reflect the trends of their contribution to the deposition rate shown in Fig.3(a). These trends can be explained by the enhancement of the secondary reactions (see Annex II) taking place at 2 Torr. As shown in Fig.4(c) H_3^+ ion flux decreases from 7.3×10^{14} cm^{-2}·s^{-1} at 2% of silane to 4.7×10^{14} cm^{-2}·s^{-1} at 10% of silane, and this trend

Tinghui Zhang *et al*

correlates with the decrease of H_3^+ ions etching rate as a function of silane concentration in Fig.3(b).

The contribution of each species to the deposition and etching rate as a function of silane concentration can also be traced back to each species production rate. Fig. 5 presents the computed time-space-averaged production rates of the

species as a function of silane concentration. As Fig.5(a) shows, the production rate of SiH_3 radicals is dominant and its trend reflects the trend in SiH_3 radicals contribution to the deposition rate. From the model, we find that SiH_3 radicals are mainly produced by the secondary reaction $SiH_4 + H = SiH_3 + H_2$ (R3 in the Annex II). As silane concentration
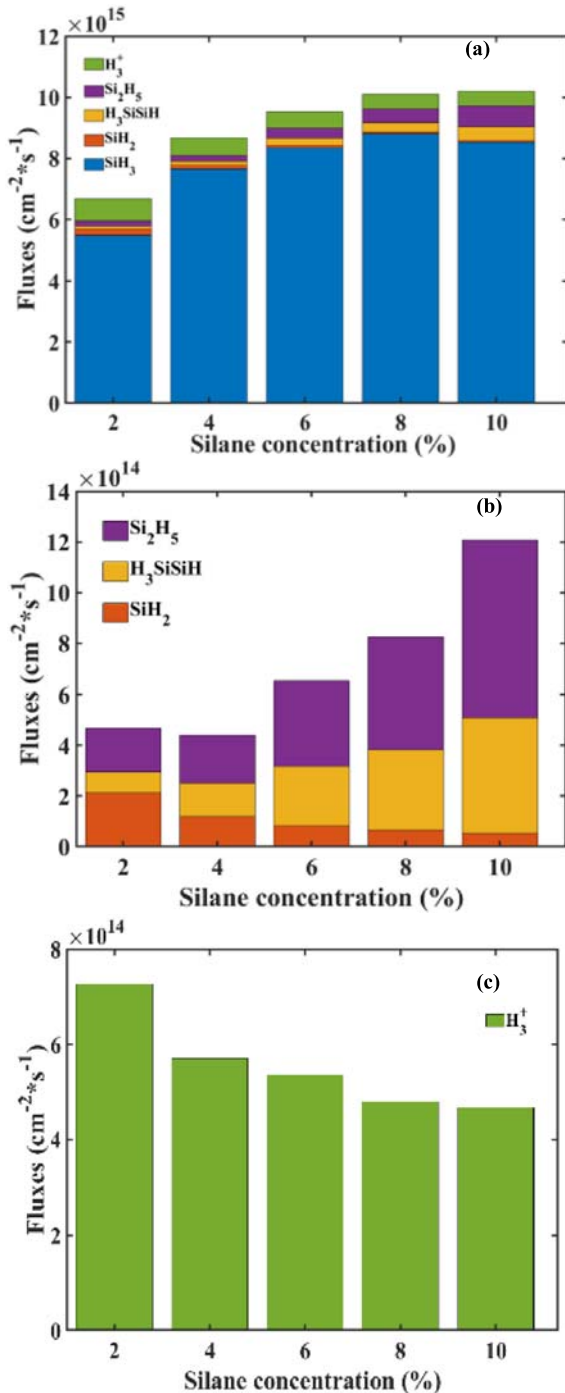

Figure 4. Computed time-averaged fluxes of the species toward the substrate as a function of silane concentration: (a) SiH_2, Si_2H_5, H_3SiSiH, SiH_3 and H_3^+; (b) radicals SiH_2, Si_2H_5, and H_3SiSiH; (c) H_3^+ ions.
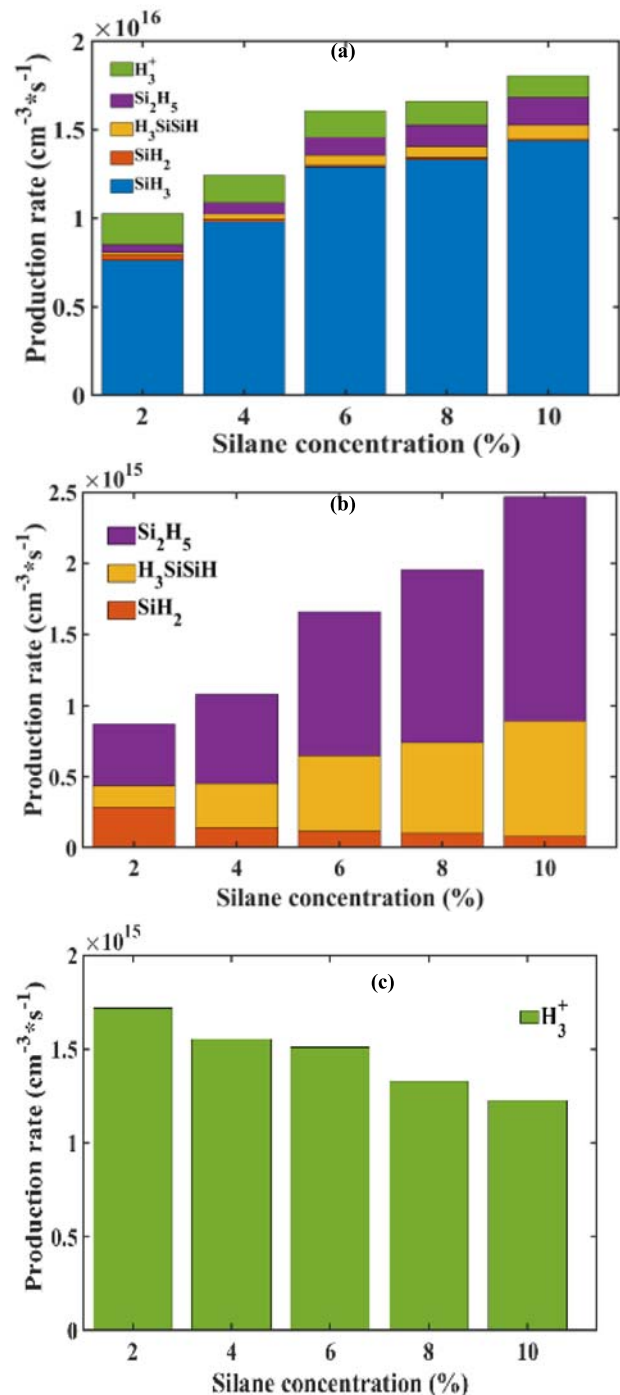
Figure 5. Computed time-space-averaged production rates of the species as a function of silane concentration: (a) SiH_2, Si_2H_5, H_3SiSiH, SiH_3 and H_3^+; (b) radicals SiH_2, Si_2H_5, and H_3SiSiH; (c) H_3^+ ions.

increases, the production rate of SiH$_3$ radicals increases from 7.6×10^{15} cm$^{-3}\cdot$s^{-1} at 2% of silane to 1.4×10^{16} cm$^{-3}\cdot$s^{-1} at 10% of silane in the gas mixture. The concentration of atomic hydrogen stays high enough with silane concentration increase, because hydrogen is always in a large excess ($\geq$ 90%). The production rates of the radicals SiH$_2$, Si$_2$H$_5$, and H$_3$SiSiH versus silane concentration are shown in Fig.5(b). We can see that the decrease in the production rate of SiH$_2$ radicals and the increase in Si$_2$H$_5$ and H$_3$SiSiH production rates reflect the trend in their contribution to the deposition rate in Fig.3(a). The main etching precursor (H$_3^+$ ions) is mainly produced via the reaction H$_2$ + H$_2^+$ = H$_3^+$ + H (see R16 in the Annex II). Its production rate as a function of silane concentration is presented in Fig.5(c). H$_3^+$ ions production rate decreases from 1.72×10^{15} cm$^{-3}\cdot$s^{-1} at 2% of silane to 1.23×10^{15} cm$^{-3}\cdot$ s^{-1} at 10% of silane and this trend reflects the decrease of H$_3^+$ ions etching rate as a function of silane concentration (see Fig.3(b)).

In summary, as silane concentration increases, the increase of experimental deposition rate values is reproduced qualitatively by the computed deposition rate quite well, despite some minor discrepancy. The difference between the computed and experimental values is considerably reduced by taking into account the etching rate. Also, we demonstrated that SiH$_3$ radicals are the main precursors for the deposition, and H$_3^+$ ions are the main contributors to the etching, each species contribution is correlated with its fluxes towards the substrate and its production rate.

4.2 Impact of gas pressure on deposition rate

In the following, we apply our model to study the effect of the gas pressure (in the range of 1.0-3.5 Torr) on the deposition rate of silicon thin films deposited on either Corning glass or c-Si substrate. For pressure series studies the following process conditions were defined: the gas temperature is fixed at 448K, the gas composition is 1.4 % SiH$_4$ + 98.6 H$_2$, the applied RF power is fixed at 10 W, the inter-electrode distance is equal to 1.6 cm. Fig.6 (a) shows the comparison between the simulated total deposition rate and corresponding experimental deposition rate at different values of total gas pressure. The trend in the experimental deposition rate on (100) crystalline silicon versus total pressure is reproduced by the computed deposition rate, however, as for the silane concentration studies, the values of the computed deposition rate are somewhat higher compared to the experimental ones. The computed deposition rate increases to a maximum of 2.6 Å/s at 2.5 Torr and then decreases to 2.2 Å/s at 3.5 Torr. In the experiments, the deposition rate has a maximum value of 1.52 Å/s at 2.75 Torr and then decreases to 1.37 Å/s at 3.5 Torr. The contributions of SiH$_3$, SiH$_2$, Si$_2$H$_5$, and H$_3$SiSiH species to the total deposition rate are also shown in Fig.6 (a). The SiH$_3$ radicals are the main precursors for silicon thin film deposition with a
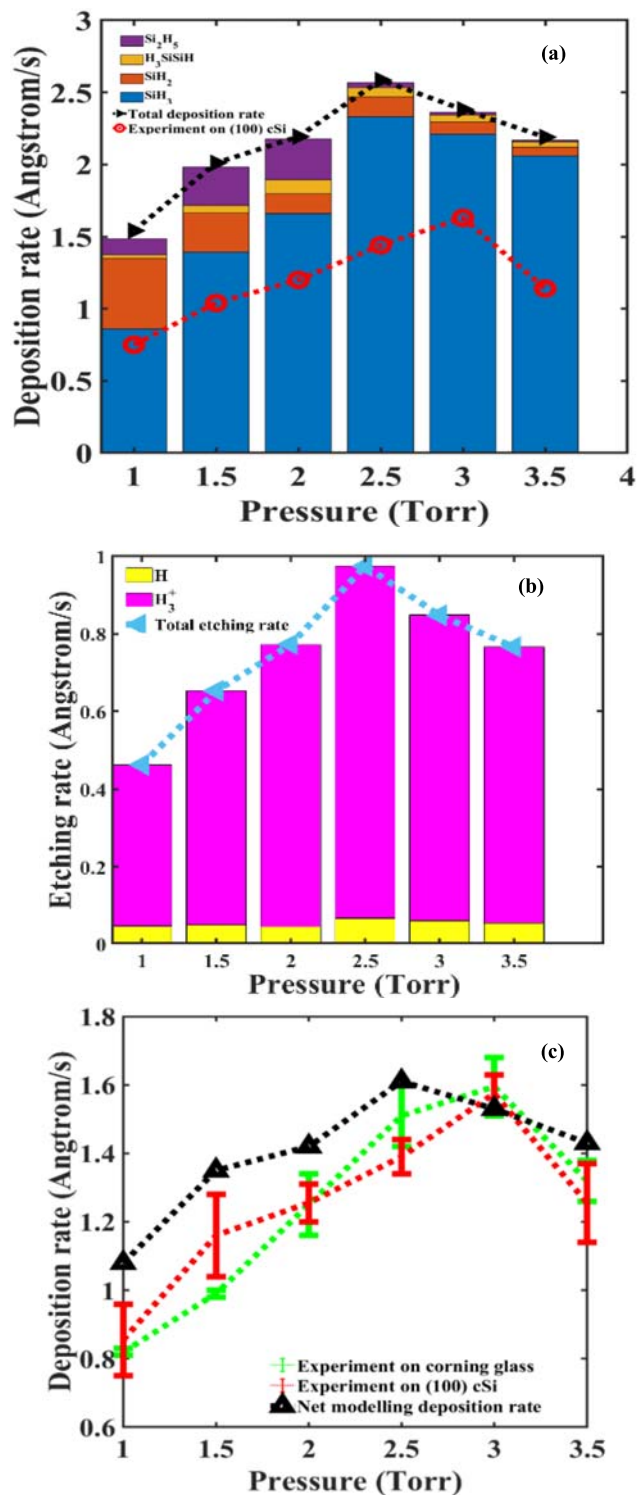
Figure 6. Deposition and etching rates versus total gas pressure: (a) experimental values of the deposition rate (red circles), simulated net deposition rate (black triangles); the histogram shows the contribution of main species to the deposition rate; (b) total etching rate, the histogram shows the contribution of different species to the etching rate. (c) computed net deposition rate (black triangles) experimental values of the deposition rate on corning glass (green dotted line) and on (100) c-Si substrate (red dotted line). The error bars are shown at each experimental pressure value.

1
2
3
4
5
6
7
8
9
10
11
12
13
14
15
16
17
18
19
20
21
22
23
24
25
26
27
28
29
30
31
32
33
34
35
36
37
38
39
40
41
42
43
44
45
46
47
48
49
50
51
52
53
54
55
56
57
58
59
60

maximum value of the corresponding deposition rate of 2.33 Å/s at 2.5 Torr that decreases to 2.06 Å/s at 3.5 Torr.

Other radicals, such as SiH_2 show a decreasing contribution to the total deposition rate as gas pressure increases. The deposition rates due to the radicals Si_2H_5 and H_3SiSiH increase to a maximum (0.28 Å/s for Si_2H_5, 0.1 Å/s for H_3SiSiH) at 2Torr, and then become negligible for pressure values above 2 Torr. The decrease of contribution of SiH_3, Si_2H_5 and H_3SiSiH radicals to the total deposition rate for pressure > 2.5 Torr is related to the drop in silane dissociation rate, as presented in Fig.7(a).
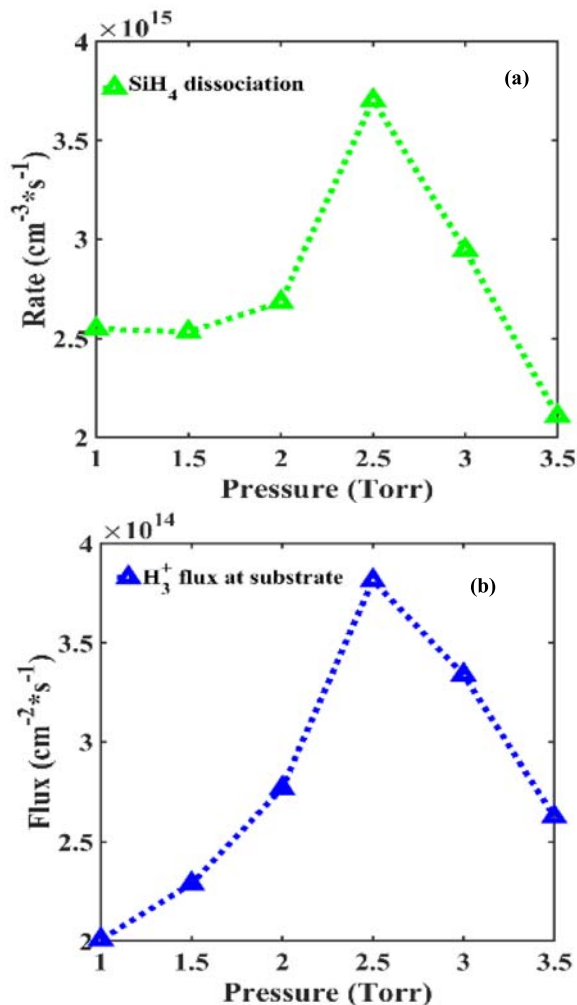
Figure 7. Computed time-space-averaged values of (a) dissociation rate of SiH_4; (b) flux of H_3^+ ions at the substrate as a function of total pressure.

The contribution of positive ions to the deposition is much smaller compared to that of radicals, for example, SiH_3^+ ions contribution ranges from 0.058 Å/s to 0.018 Å/s, which is less than 5% of the total deposition rate. Other ions, such as SiH_2^+ and $Si_2H_4^+$ also have a negligible contribution to the total deposition rate.

As for the silane concentration study, to account for the difference between the computed deposition rate and the experimental one, we consider the effect of etching by hydrogen species. Fig.6(b) presents the computed etching rate as a function of the total gas pressure. The increase in gas pressure results in an increase in the etching rate from 0.46 Å/s at 1Torr to 0.98 Å/s at 2.5Torr and a decrease to 0.77 Å/s at 3.5Torr.

As we can see in Fig. 6(b), the main precursors of etching are H_3^+ ions, which take over 90% of the etching rate. The etching rate by atomic hydrogen is much smaller; it varies from 0.05 Å/s to 0.07 Å/s and reaches a maximum at 2.5 Torr. The decrease in etching rate by H_3^+ ions for pressure values > 2.5 Torr is due to the decrease in H_3^+ ion flux at the substrate as shown in Fig.7(b).

The comparison between the computed net deposition rate and the corresponding experimental values of deposition rate on (100) crystalline silicon and Corning glass is shown in Fig.6(c). The computed net deposition rate values are close to the corresponding experimental values. Note that the deposition rate shows the same trend for the deposition on both c-Si and glass substrates. However, it is worth to mention that the structure of the films is completely different: polymorphous silicon is grown on a glass substrate and c-Si (epitaxial growth) on c-Si substrate, in agreement with our previous studies.

5. Conclusions

The 1D fluid model of capacitively coupled RF silane-hydrogen discharge developed in [22, 26] has been improved both in terms of plasma and surface chemistry to compute the deposition rate of silicon thin films. The computed deposition rates have been compared with the corresponding experimental values at different pressure and silane concentration conditions. The computed total deposition rate increases linearly with silane concentration and $SiH_3$ radicals are the main precursors of thin film deposition in the pressure range of 1 - 3.5 Torr and for silane concentrations of 2 - 10%. The computed net deposition rate shows a good agreement with the experimental values after taking into account the etching rate. Moreover, our simulations demonstrate that H_3^+ ions are the main species contributing to the etching process and their impact decreases with silane concentration. Similar results have been obtained for the studies on the effect of gas pressure on the deposition rate. It was found that the deposition rate is dominated by the contribution of SiH_3 radicals while H_3^+ ions account for an etching rate. At pressure 2.5 Torr the etching rate by H_3^+ ions is equal to 1 Å/s, which is about 40% of the total deposition rate due to the radicals (2.6 Å/s), resulting in a net deposition rate of 1.6 Å/s. After including the etching rate into the calculations of the net deposition rate the values of the latter come much closer to the experimental values.

References

[1] Roca i Cabarrocas P. , Kim K. H., Cariou R., Labrune M., Johnson E. V., Moreno M., Torres Rios A., Abolmasov S. and Kasouit S. 2012. *MRS Online Proceedings Library Archive* **1426** 319

[2] Antoine A. M., Drevillon B., and Roca i Cabarrocas P. 1985 *J. Non-Cryst. Solids* **77** 769

[3] Luft W. and Tsuo Y. S. 1993 *Hydrogenated amorphous silicon alloy deposition processes*. New York: Marcel Dekker.

[4] Street R. A. 2005 *Hydrogenated amorphous silicon* Cambridge University Press

[5] Landheer K., Goedheer W. J., Poulios I., Schropp R. E. I. and Rath J. K. 2016 *J. Appl. Phys.* **120** 053304

[6] Nienhuis G. J., Goedheer W. J., Hamers E. A. G., Van Sark W. G. J. H. M. and Bezemer J. 1997 *J. Appl. Phys.*, **82** 2060

[7] Leroy O., Gousset G., Alves L. L., Perrin J. and Jolly J. 1998 *Plasma Sources Sci. Technol.* **7** 348

[8] Howling A. A., Legradic B., Chesaux M. and Hollenstein C. 2012 *Plasma Sources Sci. Technol.* **21** 015005

[9] Kushner M. J. 1986 *MRS Online Proceedings Library Archive* **68** 293

[10] Leal R, Bruneau B., Bulkin P., Novikova T., Silva, F., Habka N., Johnson E. 2020 *Plasma Sources Sci. Technol.* **29** (2), 025023

[11] Roca i Cabarrocas P., Nguyen-Tran T., Djeridane Y., Abramov A., Johnson E. and Patriarche G. 2007 *J. Phys. D: Appl. Phys.*, **40** 2258

[12] Roca i Cabarrocas P., i Morral A. F., Lebib S. and Poissant Y. 2002 *Pure Appl. Chem.* **74** 359

[13] Amanatides E., Stamou S. and Mataras D. 2001 *J. Appl. Phys.* **90** 5786

[14] Perrin J., Leroy O. and Bordage M. C. 1996 *Contrib. to Plasma Phys.* **36** 3

[15] Perrin J., Shiratani M., Kae-Nune P., Videlot H., Jolly J. and Guillon J. 1998 *J. Vac. Sci. Technol. A* **16** 278

[16] Perrin J. and Broekhuizen T. 1987 *Appl. Phys. Lett.* **50** 433

[17] Tsalikis D. G., Baig C., Mavrantzas V. G., Amanatides E. and Mataras D. 2013 *J. Chem. Phys.* **139** 204706

[18] Alves L. L. and Marques L. 2012 *Plasma Physics and Controlled Fusion* **54** 124012

[19] Roca i Cabarrocas P., Chévrier J. B., Huc J., Lloret A., Parey J. Y. and Schmitt J. P. M. 1991 *J. Vac. Sci. Technol. A* **9** 2331

[20] Fontcuberta i Morral A., Roca i Cabarrocas P. and Clerc C. 2004 *Phys. Rev. B* **69** 125307

[21] Roca i Cabarrocas P., Hamma S., Hadjadj A., Bertomeu J. and Andreu J. 1996 *Appl. Phys. Lett.* **69** 529

[22] Orlac'h J. M., Novikova T., Giovangigli V., Johnson E. and Roca i Cabarrocas P. 2019 *Plasma Sources Sci. Technol.* **28** 055003

[23] Graves D. B. and Jensen K. F. 1986 *IEEE Trans. Plasma Sci.* **14** 78

[24] Boeuf J. P. and Belenguer P. 1992 *J. Appl. Phys.* **71** 4751

[25] De Bleecker K., Bogaerts A., Goedheer W., and Gijbels R. 2004 *IEEE Trans. Plasma Sci.* **32** 691

[26] Orlac'h J. M. 2017.Modeling of a silane-hydrogen plasma discharge including nanoparticle dynamics for photovoltaic applications (PhD dissertation, University Paris Saclay).

[27] Giovangigli V. 2012 *Sci. China Math.* **55** 285

[28] Oran E. S., Boris J. P. 1981 *Prog. Energy Combust. Sci.* **7** 1.

[29] Mortimer R. G. and Eyring H. *Proc. Natl. Acad. Sci.* **77** 1728

[30] Ern A. and Giovangigli V. 2009 EGLIB server and User's manual (http://cmap.polytechnique.fr/www.eglib/)

[31] Kee R. J., Dixon-Lewis G., Warnatz J., Coltrin M. E. and Miller J. A. 1986 A Fortran computer code package for the evaluation of gas-phase multicomponent transport properties. *Sandia National Laboratories Report SAND86-8246*, **13** 80401

[32] Hagelaar G.J.M. and Pitchford L. C. 2013 *Proc. APS Gaseous Electronics Conference*, MR1-075.

[33] A. V. Phelps database, University of Colorado Boulder (www.lxcat.net/Phelps)

[34] Yoon J. S., Song M. Y., Han J. M., Hwang S. H., Chang W. S., Lee B. and Itikawa Y. 2008 *J. Phys. Chem. Ref. Data* **37** 913

[35] Kim Y. K. and Rudd M. E. 1994 *Phys. Rev. A* **50** 3954

[36] Janev R. K., Langer W. D., Evans J. K. and Post J. D. E. 1987 *Elementary Processes in Hydrogen-Helium Plasmas* Springer-Verlag New York.

[37] Krishnakumar E. and Srivastava S. K. 1995 *Contrib. to Plasma Phys.* **35** 395

[38] Tarnovsky V., Deutsch H. and Becker K. 1996 *J. Chem. Phys.* **105** 6315

[39] Dance D. F., Harrison M. F. A., Rundel R. D. and Smith A. C. H. 1967 *Proc. Phys. Soc.* **92** 577

[40] Peart B. and Dolder K. T. 1974 *J. Phys. B: At. Mol Phys* **7** 236

[41] Peart B. and Dolder K. T. 1975 *J. Phys. B: At. Mol. Phys.* **8** 1570

[42] Peart B. and Dolder K. T. 1974 *J. Phys. B: At. Mol. Phys.* **7** 1948

[43] Haaland P. 1990 J. *Chem. Phys.* **93** 4066

[44] Nalwa H. S. 2002 *Handbook of thin film materials*. Academic Press.

[45] Diomede P., Longo S., Economou D. J. and Capitelli M. 2012 *J. Phys. D: Appl. Phys.* **45** 175204

[46] Chapman S. and Cowling T. G. 1970 *The Mathematical Theory of Non-Uniform Gases* 3rd Ed. Cambridge University Press

[47] Kleijn C. R. 2000 *Thin Solid Films* **365** 294

[48] Ke, R. J., Coltrin M. E. and Glarborg P. 2005 *Chemically reacting flow: theory and practice* John Wiley & Sons

[49] Motz H. and Wise H. 1960 *J. Chem. Phys.* **32** 1893

[50] Patankar S. V., Minkowycz W. J. and Sparrow E. M. 1980 *Series in computational methods in mechanics and thermal sciences.* McGraw-Hill Book Company, New York, 1-197

[51] Atkinson K. E. 2008 *An introduction to numerical analysis* John Wiley & Sons

[52] Scharfetter D. L. and Gummel H. K. 1969 *IEEE Trans. Electron Devices* **16** 64

[53] Kim K. H., Johnson E. V., Kazanskii A. G., Khenkin M. V. and Roca i Cabarrocas P. 2017 *Sci. Rep.* **7** 1

[54] Kail F., Fontcuberta i Morral A., Hadjadj A., Roca i Cabarrocas P., and Beorchia A. 2004 *Philos. Mag.* **84** 595

[55] Fontcuberta i Morral A. and Roca i Cabarrocas P. 2006 *EPJ Appl. Phys.* **35** 165

[56] Kim Y. K. and Rudd M. E. 1994 *Phys. Rev. A* **50** 3954

[57] Scott C. D., Farhat S., Gicquel A., Hassouni K. and Lefebvre M. *J. Thermophys. Heat Trans.* **10** 426

[58] Janev R. K., Langer W. D., Post D. E. and Evans K. 1987 *Elementary Processes in Hydrogen-Helium Plasmas* (pp. 17-114). Springer, Berlin, Heidelberg.

[59] Bhandarkar U. V., Swihart M. T., Girshick S. L. and Kortshagen U. R. 2000 *J. Phys. D: Appl. Phys.* **33** 2731

[60] Kalache B., Novikova T., Fontcuberta i Morral A., Roca i Cabarrocas P., Morscheidt W. and Hassouni K. 2004 *J. Phys. D: Appl. Phys.* **37** 1765

[61] Coltrin M. E., Kee R. J. and Miller J. A. 1986 *J. Electrochem. Soc.* **133** 1206

[62] Coltrin M., Kee R., Evans G. and Miller G. 1987 *Proc. 10th International Conference on CVD* (p. 33).

Annex I. Electron collision reactions included in the plasma chemistry model

Reaction number	Electron collision	A_r (mol, cm^3, s)	β_r	$\mathfrak{E}_r$ (cal.mol^{-1})	*Ref.*
	Ionization				
R1	$H_2 + e => H_2^+ + 2e$	4.798×10^{13}	0.505	361,455	[33]
R2	$H + e => H^+ + 2e$	1.080×10^{16}	0	178,210	[56]
R3	$H_2 + e => H^+ + H + 2e$	3.745×10^{10}	0.810	418,729	[58]
R4	$SiH_4 + e => SiH_3^+ + H + 2e$	1.510×10^{32}	-2.930	553,910	[59]
R5	$SiH_3 + e => SiH_3^+ + 2e$	1.355×10^{12}	0.900	188,396	[59]
	Dissociation				
R6	$H_2 + e => 2H + e$	1.020×10^{16}	0	238,347	[33]
R7	$H_3^+ + e => H^+ + 2H + e$	1.220×10^{17}	0	179,380	[57]
R8	$H_2^+ + e => H^+ + H + e$	1.460×10^{17}	0	37,460	[57]
R9	$SiH_4 + e => SiH_3 + H + e$	1.1×10^{21}	-1.000	245,421	[59]
R10	$SiH_4 + e => SiH_2 + 2H + e$	5.4×10^{21}	-1.000	245,421	[59]
	Dissociative attachment				
R11	$SiH_4 + e => SiH_3^- + H$	2.269×10^{21}	-1.627	190,540	[59]
R12	$SiH_4 + e => SiH_2^- + 2H$	2.269×10^{21}	-1.627	190,540	[59]
R13	$SiH_3 + e => SiH_2^- + H$	3.440×10^{15}	-0.500	44,740	[59]
	Detachment				
R14	$SiH_3^- + e => SiH_3 + 2e$	1.900×10^{14}	0.500	32,425	[59]
R15	$SiH_2^- + e => SiH_2 + 2e$	1.900×10^{14}	0.500	25,921	[59]
	Recombination and dissociative recombination				
R16	$H^+ + 2e \rightarrow H + e$	3.630×10^{37}	-4.000	0	[57]
R17	$H_3^+ + e \rightarrow 3H$	8.000×10^{17}	-0.404	0	[57][60]
R18	$H_3^+ + 2e \rightarrow H + H_2 + e$	3.170×10^{21}	-4.500	0	[57]
R19	$H_2^+ + 2e \rightarrow 2H + e$	3.170×10^{21}	-4.500	0	[57]

Annex II. Heavy species reactions included in the plasma chemistry model

Reaction number	Heavy species reactions	A_r (mol, cm^3, s)	β_r	$\mathfrak{E}_r$ (cal.mol^{-1})	*Ref.*
	Neutral-neutral reactions				
R1	$H_2 + H_2 = 2H + H_2$	8.610×10^{17}	-0.700	52,530	[57]
	Reverse rate	1.000×10^{17}	-0.600	0.0	[57]
R2	$H_2 + H = 3H$	2.700×10^{16}	-0.100	52,530	[57]
	Reverse rate	3.200×10^{15}	0	0.0	[57]
R3	$SiH_4 + H = SiH_3 + H_2$	1.51×10^{13}	0	2,484	[59]
R4	$Si_2H_6 + H = Si_2H_5 + H_2$	1.3×10^{12}	0	0	[59]
R5	$Si_2H_6 + H = SiH_3 + SiH_4$	4.82×10^{13}	0	2,484	[59]
R6	$SiH_2 + H_2 = SiH_4$	5.260×10^{10}	0.000	0	[59]
R7	$SiH_2 + SiH_4 = Si_2H_6$	3.620×10^{13}	0.000	0	[59]
R8	$SiH_3 + SiH_3 = SiH_2 + SiH_4$	9.03×10^{13}	0.000	0	[59]
	Neutralization reaction				
R9	$SiH_3^- + SiH_3^+ = SiH_3 + SiH_3$	1.232×10^{18}	-0.500	0	[59]
R10	$SiH_2^- + SiH_3^+ = SiH_2 + SiH_3$	1.359×10^{18}	-0.500	0	[59]
R11	$Si_2H_5^- + SiH_3^+ = Si_2H_5 + SiH_3$	9.648×10^{17}	-0.500	0	[59]
R12	$H_3SiSiH^- + SiH_3^+ = H_3SiSiH + SiH_3$	1.001×10^{18}	-0.500	0	[59]
	Cluster growth				
R13	$SiH_3^- + SiH_4 = Si_2 \ H_5^- + H_2$	6.020×10^{11}	0.000	0	[59]
R14	$SiH_2^- + SiH_4 = H_3SiSiH^- + H_2$	6.020×10^{11}	0.000	0	[59]
	Additional hydrogen reactions				
R15	$H_2^+ + H = H^+ + H_2$	3.850×10^{14}	0.000	0	[57][60]
	Reverse rate	1.900×10^{14}	0.000	21,902	[57]
R16	$H_2 + H_2^+ \rightarrow H_3^+ + H$	1.270×10^{15}	0.000	0	[57][60]
R17	$H^+ + 2H_2 \rightarrow H_3^+ + H_2$	1.950×10^{20}	-0.500	0	[57][60]

Annex III. List of the surface reactions. Notation (g) means gas species; notation (s) means surface species; notation wall means substrate. ϱ, ε, and σ represent the probabilities of recombination, etching and sticking, respectively. The sticking coefficients for hydrogen and its ions are taken equal to 0.0.

Reaction number	surface reactions	p_r (-)	*Ref.*
R1	H + wall= 0.5H$_2$ (g)	$\varrho_H = 0.7$	[15][16]
R2	4H+ Si-wall = SiH$_4$(g)	$\varepsilon_H = 3.045 \cdot 10^{-4} \exp(1357/T_s)$ *(T$_s$ is the substrate temperature)*	[15][29][7]
R3	4H$^+$ +Si-wall= SiH$_4$(g)	$\varepsilon_{H^+} = 1.0$	[7]
R4	2H$_2$$^+$ + Si-wall =SiH$_4$(g)	$\varepsilon_{H_2^+} = 1.0$	[7]
R5	4H$_3$$^+$ + 3Si-wall = 3SiH$_4$ (g)	$\varepsilon_{H_3^+} = 1.0$	[7]
R6	SiH$_2$(g) +wall= Si(s) +H$_2$(g)	$\sigma_{SiH_2} = 0.8$	[15][16]
R7	SiH$_3$(g)+wall=Si(s)+H$_2$(g)+H(g)	$\sigma_{SiH_3} = 0.1$	[15][16]
R8	SiH$_3$(g) + SiH$_3$-wall = Si$_2$H$_6$(g)	$\varrho_{SiH_3 \rightarrow Si_2H_6} = 0.0$	[15][16]
R9	SiH$_3$(g)+H-wall=SiH$_4$(g)	$\varrho_{SiH_3} = 0.16$	[15][16]
R10	SiH$_4$(g)+wall=Si(s)+2H$_2$(g)	$\sigma_{SiH_4} = 5.37 \cdot 10^{-2} \exp(-9400/(RT_s))$	[61]
R11	H$_3$SiSiH(g)+wall=2Si(s)+2H$_2$(g)	$\sigma_{Si_2H_4} = 0.8$	[15][16]
R12	Si$_2$H$_5$(g) + wall= 2Si(s) + 2H$_2$(g) + H(g)	$\sigma_{Si_2H_5} = 0.1$	[15][16]
R13	Si$_2$H$_5$(g)+ H-wall= Si$_2$H$_6$(g)	$\varrho_{Si_2H_5} = 0.16$	[15][16]
R14	Si$_2$H$_6$(g) + wall=2Si(s) +3H$_2$(g)	$\sigma_{Si_2H_6} = 5.37 \cdot 10^{-1} \exp(-9400/(RT_s))$	[62]
R15	SiH$_3$$^+$ + wall=Si(s)+H$_2$(g)+H(g)	$\sigma_{SiH_3^+} = 1.0$	[14]
R16	SiH$_2$$^+$ + wall =Si(s)+H$_2$(g)	$\sigma_{SiH_2^+} = 1.0$	[14]
R17	Si$_2$H$_4$$^+$ + wall = 2Si (s)+ 2H$_2$(g)	$\sigma_{Si_2H_4^+} = 1.0$	[14]